Neuron

NeuroResource

An implantable device for wireless monitoring of diverse physio-behavioral characteristics in freely behaving small animals and interacting groups

Highlights

- A wireless, battery-free implant captures diverse mechano-acoustic signals
- Advanced algorithms robustly parse out physiological and behavioral parameters
- It reveals physio-behavioral coordination under stress and optogenetic stimulation
- It offers continuous, chronic monitoring of circadian rhythms

Authors

Wei Ouyang, Keith J. Kilner, Rachael M.P. Xavier, ..., Sam A. Golden, Cameron H. Good, John A. Rogers

Correspondence

sagolden@uw.edu (S.A.G.), cameron.good@northwestern.edu (C.H.G.), jrogers@northwestern.edu (J.A.R.)

In brief

Ouyang et al. report a wireless, battery-free implant for comprehensive, continuous monitoring of physiology and behavior in freely behaving small animals and interacting groups. Demonstrations in pharmacological, locomotor, and acute and social stress tests and the implant's concurrent operation with wireless optogenetics showcase its broad utility as a tool for neuroscience.

Ouyang et al., 2024, Neuron *112*, 1–14
June 5, 2024
https://doi.org/10.1016/j.neuron.2024.02.020

CellPress

Neuron

CellPress

NeuroResource

An implantable device for wireless monitoring of diverse physio-behavioral characteristics in freely behaving small animals and interacting groups

Wei Ouyang,[1,2] Keith J. Kilner,[1,3] Rachael M.P. Xavier,[3] Yiming Liu,[1] Yinsheng Lu,[1] Sophia M. Feller,[3] Kayla M. Pitts,[4] Mingzheng Wu,[1] Jokubas Ausra,[3] Ian Jones,[3] Yunyun Wu,[1] Haiwen Luan,[1] Jacob Trueb,[1] Elizabeth M. Higbee-Dempsey,[5] Iwona Stepien,[5] Nayereh Ghoreishi-Haack,[5] Chad R. Haney,[6] Hao Li,[7,8] Yevgenia Kozorovitskiy,[9,10] Mitra Heshmati,[4,11,12] Anthony R. Banks,[1,3] Sam A. Golden,[4,11,*] Cameron H. Good,[1,3,*] and John A. Rogers[1,13,14,15,16,17,18,*]

[1]Querrey Simpson Institute for Bioelectronics, Northwestern University, Evanston, IL 60208, USA
[2]Thayer School of Engineering, Dartmouth College, Hanover, NH 03755, USA
[3]NeuroLux Inc., Northfield, IL 60093, USA
[4]Department of Biological Structure, University of Washington, Seattle, WA 98195, USA
[5]Developmental Therapeutics Core, Northwestern University, Evanston, IL 60208, USA
[6]Center for Advanced Molecular Imaging, Northwestern University, Evanston, IL 60208, USA
[7]Department of Psychiatry and Behavioral Sciences, Feinberg School of Medicine, Northwestern University, Evanston, IL 60208, USA
[8]Department of Neuroscience, Feinberg School of Medicine, Northwestern University, Evanston, IL 60208, USA
[9]Department of Neurobiology, Northwestern University, Evanston, IL 60208, USA
[10]Chemistry of Life Processes Institute, Northwestern University, Evanston, IL 60208, USA
[11]Center of Excellence in Neurobiology of Addiction, Pain, and Emotion (NAPE), University of Washington, Seattle, WA 98195, USA
[12]Department of Anesthesiology and Pain Medicine, University of Washington, Seattle, WA 98195, USA
[13]Department of Materials Science and Engineering, Northwestern University, Evanston, IL 60208, USA
[14]Department of Mechanical Engineering, Northwestern University, Evanston, IL 60208, USA
[15]Department of Biomedical Engineering, Northwestern University, Evanston, IL 60208, USA
[16]Department of Chemistry, Northwestern University, Evanston, IL 60208, USA
[17]Department of Neurological Surgery, Feinberg School of Medicine, Northwestern University, Evanston, IL 60208, USA
[18]Lead contact
*Correspondence: sagolden@uw.edu (S.A.G.), cameron.good@northwestern.edu (C.H.G.), jrogers@northwestern.edu (J.A.R.)
https://doi.org/10.1016/j.neuron.2024.02.020

SUMMARY

Comprehensive, continuous quantitative monitoring of intricately orchestrated physiological processes and behavioral states in living organisms can yield essential data for elucidating the function of neural circuits under healthy and diseased conditions, for defining the effects of potential drugs and treatments, and for tracking disease progression and recovery. Here, we report a wireless, battery-free implantable device and a set of associated algorithms that enable continuous, multiparametric physio-behavioral monitoring in freely behaving small animals and interacting groups. Through advanced analytics approaches applied to mechano-acoustic signals of diverse body processes, the device yields heart rate, respiratory rate, physical activity, temperature, and behavioral states. Demonstrations in pharmacological, locomotor, and acute and social stress tests and in optogenetic studies offer unique insights into the coordination of physio-behavioral characteristics associated with healthy and perturbed states. This technology has broad utility in neuroscience, physiology, behavior, and other areas that rely on studies of freely moving, small animal models.

INTRODUCTION

The brain centrally encodes intricately orchestrated peripheral physiological processes and behavioral states, essential to sustain life and to respond to external stimuli.[1] The midbrain periaqueductal gray, for example, coordinates defensive responses to threats by regulating peripheral changes in cardiac activities (e.g., tachycardia, bradycardia) and patterns of behavior (e.g., fight, flee).[2–4] Simultaneous, quantitative monitoring of parameters of physiology and behavior can, thus, facilitate studies of underlying neural circuits and their functions. Comprehensive assessments of these physio-behavioral characteristics also yield measurable indicators of neurological and psychiatric states, along with basic health status. Such data may further reveal biomarkers associated with specific diseases, define the efficacy and side effects of pharmacological agents, and quantitatively monitor disease progression and recovery. Collectively, systems for simultaneous physio-behavioral monitoring offer

Please cite this article in press as: Ouyang et al., An implantable device for wireless monitoring of diverse physio-behavioral characteristics in freely behaving small animals and interacting groups, Neuron (2024), https://doi.org/10.1016/j.neuron.2024.02.020

significant promise as tools for neuroscience research, drug development, and understanding of disease states.

The development of wireless, multiparametric sensors that are compatible with small animal models, and bypass the limitations associated with tethered approaches, represents a daunting technical challenge.[5–7] Existing hardware approaches combine standalone sensors for physiological processes (cardiopulmonary activity, temperature, and other body functions) with camera systems for body movements and behaviors.[3] As summarized in Table S1, the most advanced technologies for the former, being wireless and fully implantable to allow for social interactions and/or free movement in three-dimensional environments, support physiological monitoring by electrocardiography (ECG) and photoplethysmography (PPG), but without capabilities for monitoring behavioral states. These devices also have a set of disadvantages that include battery-powered operation, bulky form factors, and excessive masses, which collectively can modify naturalistic behaviors and constrain experimental paradigms; they also are limited for use only in single or a few animals.[8–12] Computer vision is a powerful option[13] for the latter, but applicable only to video that provides a direct line of sight. Due to camera positioning, resolution, framerate, and data storage and analysis requirements, additional limitations are common when identifying subtle behaviors, monitoring similar-looking animals, or observing naturalistic behaviors in enriched, multi-animal environments.[13,14] The combined use of discrete physiology sensing devices and camera systems complicates the experimental apparatus and procedures. Challenges also arise around precise time synchronization of signals from individual sensors, especially wireless ones, to sub-millisecond resolution, a critical requirement for pairing with the rapidly evolving tools used to measure neural activity dynamics.[15,16] Integrated capabilities for multiparametric physio-behavioral monitoring via a single wireless, battery-free, soft, lightweight, and miniaturized device that can be fully implanted into the animal represents an unrealized ideal for neuroscience and biomedical research of individual subjects or interacting groups.

The solution introduced here exploits the multitude of mechano-acoustic (MA) signals associated with natural body processes in small animals as a diverse source of physiological and behavioral information.[17] Examples include vocalizations (~1–100 kHz), cardiac activities (rate and amplitude; ~10–100 Hz), blood flow (~1–1,000 Hz), respiratory movements (rate and amplitude, ~1 Hz) and sounds (~100–1,000 Hz), gastrointestinal processes (~0.01–0.1 Hz), and body orientation and locomotion (~0.1–10 Hz).[18,19] Small-form microelectromechanical systems (MEMSs) serve as inertial measurement units (IMUs) for MA sensing across a full spectrum of frequencies, from the mechanical to the acoustic regimes. IMUs interfaced to the body through optimized mechanics designs efficiently capture MA signals from within the body. Ambient noise does not contribute to these signals because air-transmitted sounds do not have sufficient mechanical power to drive notable vibrations of the implanted IMUs.[20–22] Recent work demonstrates the utility of the MA approach in humans using epidermal MA devices for monitoring physiological processes for a broad range of applications.[20–22] Thus, similar sensing mechanisms applied to small animals have the potential to offer related multiparametric, intrinsically synchronized physio-behavioral data (Figure 1A). The technical difficulties are in achieving devices with (1) sufficiently small sizes and masses that effectively eliminate burdens on the animals or restrictions on their naturalistic behaviors, (2) conformal, intimate tissue interfaces that efficiently couple the device to the various subtle acousto/mechanical processes that occur in freely behaving animals, and (3) time series data of a quality that allows accurate analysis of physio-behavioral patterns in isolated animals or socially interacting groups. Existing wireless IMU-integrated devices for small animals fail to offer these attributes, and they involve additional technical limitations detailed previously.[23–25] Aside from hardware design, existing algorithms for MA signal processing do not provide reliable separation of physiological information from movement, thereby limiting their uses for freely behaving animals.[20–22]

This paper reports a collection of advances in materials science, electrical engineering, data analytics, and surgical procedures that successfully address these challenges in the form of a fully implantable, wireless device. The technology allows for synchronous determination of physiological and behavioral information during free movements of mouse and rat models, including heart rate (HR), respiratory rate (RR), physical activity (PA), temperature, and various behavioral states (resting, eating, walking, rearing, grooming, and digging), without measurable constraints on locomotion or other natural activities. Demonstrations in pharmacological, running wheel, forced swim, shock grid, resident-intruder, and witness defeat tests illustrate a broad set of representative applications relevant to studies in neuroscience and biomedicine. Chronic, continuous monitoring in a freely behaving mouse for 17 days, reveals circadian effects on physio-behavioral characteristics as a demonstration of the reliability and stability of operation necessary for research across various temporal scales. Integration into animals implanted with a separate wireless optogenetic device provides an opportunity to monitor physiological changes during optogenetic manipulation of neural circuits.

RESULTS

Design concepts, engineering mechanics, and system features

The flexible, lightweight device includes a small-footprint, high-bandwidth MEMS 6 axis IMU (BMI160, Bosch Sensortec, Germany), a miniaturized temperature sensor (MAX31875, Analog Devices), wireless electronics, and wireless power transfer (WPT) circuitry on a flexible printed circuit board (fPCB) for implantation in the subdermal area of the ventral side of an animal (mice and rats, Figure 1B). Figure S1A shows the surgical procedures. Because MA signals attenuate strongly through the tissue and across interfaces between tissues and surrounding biofluid, the IMU portion of the device must adhere conformally and firmly to a thin layer of muscle on the sternum in the vicinity of the heart to ensure efficient mechanical coupling (Figure 1B). Other body locations (e.g., dorsal) or surgical procedures that fail to form an intimate interface with the body cannot support adequate, consistent measurements due to attenuation and time variability in the MA signals (Figures S1B–S1D). The IMU

Please cite this article in press as: Ouyang et al., An implantable device for wireless monitoring of diverse physio-behavioral characteristics in freely behaving small animals and interacting groups, Neuron (2024), https://doi.org/10.1016/j.neuron.2024.02.020

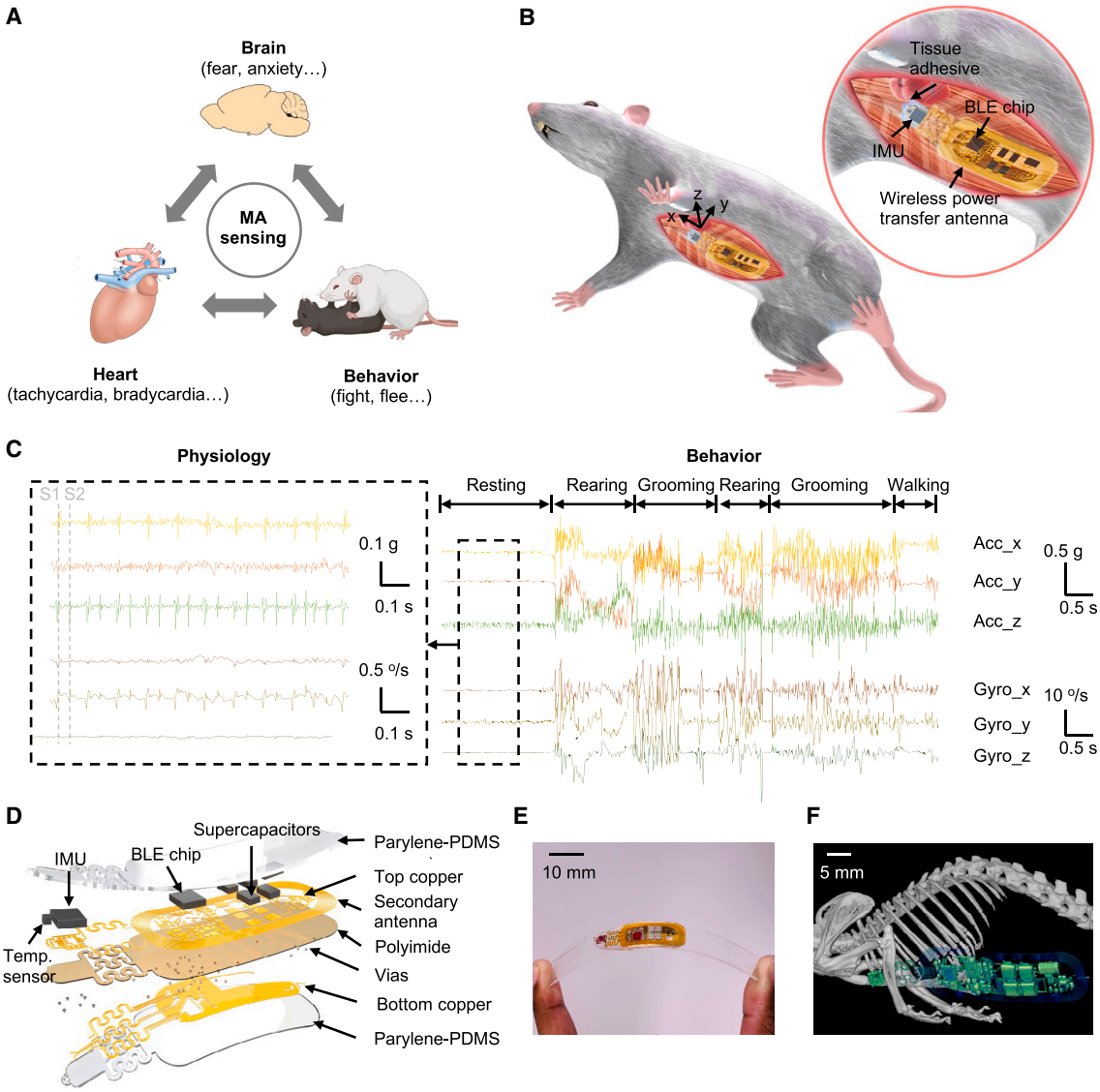

Figure 1. System concept, device design, and implant location

(A) Schematic illustration of a battery-free mechano-acoustic sensing system as a fully implantable, wireless monitor for physiological processes and behavioral patterns in freely moving mice.

(B) Schematic illustration of a device implanted in the subdermal area of the ventral side of a mouse to ensure efficient coupling to mechano-acoustic signatures of body processes.

(C) Representative broadband accelerometer and gyroscope data wirelessly captured from a freely moving mouse.

(D) Exploded view illustration of the device.

(E) Photograph of a device under bending.

(F) Micro-CT image of a device implanted in a mouse.

resides on an island and connects to the supporting electronics by serpentine conductive traces to offer maximal flexibility for precision positioning of the IMU over the heart. Embedding the IMU on the device does not substantially alter its mechanical response as compared with a standalone IMU (Figures S1E–S1G), thereby ensuring high-fidelity recording of MA signals.

Figure 1C shows representative synchronous data from the IMU, collected from a freely moving CD1 mouse, where the z axis is normal to the surface of the chest and the x axis and y axis are along and normal to the midline of the body (Figure 1B), respectively. While resting, MA signals associated with the S1 and S2 heart sounds of each cardiac cycle appear clearly. Chest wall movements associated with respiration modulate the amplitudes of these cardiac signals in an expected manner.[26] In addition to cardiopulmonary tracking (HR and RR), other unique features in the MA data correspond to rearing, grooming, walking, and other characteristic activities as the basis for behavioral

Please cite this article in press as: Ouyang et al., An implantable device for wireless monitoring of diverse physio-behavioral characteristics in freely behaving small animals and interacting groups, Neuron (2024), https://doi.org/10.1016/j.neuron.2024.02.020

monitoring. Advanced signal processing algorithms, as discussed in the following sections, enable the concurrent extraction of these various classes of information from the MA signals.

Electrical and mechanical design attributes

As presented in Figures 1D, S1H, and S1I, the device comprises a vertical assembly of electrical components, a double-layer fPCB, and parylene-poly(dimethylsiloxane) (PDMS) encapsulation structures at the top and bottom. Parylene and PDMS are widely used biocompatible materials for encapsulating implantable devices, which generate minimal immune responses.[27–31] The MA sensing and temperature sensing occur at 800 and 0.1 Hz, respectively, with continuous wireless communication by a Bluetooth-low-energy (BLE) system-on-a-chip. WPT by resonant magnetic inductive coupling supports device operation (Figures S2A and S2B) through a near-field communication (NFC, 13.56 MHz) radio frequency (RF) power distribution system, a double-loop primary antenna encircling the experimental arena (30 × 20 × 20 cm [length × width × height]), and a secondary antenna tuned to 13.56 MHz on the device. The AC voltage induced on the secondary antenna passes through a full-wave bridge rectifier to yield a stable DC voltage of 2.5 V through a low-dropout (LDO) regulator. The device consumes 2.7 mW in the accelerometer-only mode (Figure S2C) and 4.6 mW in the accelerometer-gyroscope mode. To maximize stability of operation, the device works in the accelerometer-only mode when implanted in animals, unless otherwise specified. A challenge with WPT arises from angular misalignment between the primary and secondary antennae during rearing behaviors. As shown in Figures S2D–S2O, the power received decreases with the rearing angle, with 2.7 and 4.2 mW received at 75° under RF input powers of 6 and 10 W, respectively. An array of four supercapacitors (7.5 mF each), continuously charged by WPT, serve as a temporary source of power to support transient operation for up to 30 s for angles greater than 75°. WPT causes a local temperature increase of less than 0.6°C and 1.3°C at the AC-DC conversion circuitry in air (Figures S2P and S2Q) under RF input powers of 6 W (typical operational condition) and 10 W (maximum power), respectively, within the limit of a chronic temperature increase of 2 °C for implanted devices recommended by the American Association of Medical Instrumentation.[32] The temperature sensor resides on an externalized island from the main device body (Figure 1D) and is not subject to artifacts from WPT heating. A water bath test suggests that the temperature sensor, encapsulated in PDMS, precisely records ambient temperature, with a correlation of >0.999 with an unencapsulated commercial thermocouple located in the vicinity of the device (Figure S2R). Figure 1E shows a photograph of a completed device under bending that simulates expected levels of deformation when implanted on the ventral side of a mouse. Computed tomography (CT) images (Figure 1F) collected 2 weeks after surgery indicate that the devices remain in their original positions, with no signs of degradation in functionality or appearance. Dislocation of the IMU, which might compromise the signal quality, does not occur over the course of 8 weeks, when animals freely engaged in different behaviors. The devices, when outsource manufactured, maintain full functionality in freely behaving animals for at least 8 weeks (Figure S3). When hand manufactured, the devices fail by fracture of some solder joints of the BLE chip following repetitive bending in the body (Figure S3B), as discussed in detail in our previous publication on a different, but related, technology.[12]

Signal processing algorithms

MA signals superpose physiological and behavioral information from a multitude of sources. Algorithms that exploit the characteristic time-frequency features of various body processes allow for separate determination of multiple physiological and behavioral parameters during both periods of resting and PA.

MA signals associated with heart sounds have relatively high frequency content (>∼25 Hz). This feature provides a theoretical basis for reliable separation from body movements, which are dominated by relatively low frequencies (<∼25 Hz). By contrast, measurements that exploit PPG data rely on pulse cycles (<∼15 Hz for mice) that are in spectral overlap with body movements, thereby rendering a high sensitivity to motion artifacts.[33] Despite the dominant frequencies of heart sounds and body movements being separate, body movements still include higher-order components that spectrally overlap with those of heart sounds. Thus, simple digital bandpass filtering and denoising techniques (e.g., wavelet transforms) do not entirely separate heart sounds from movements[34] (Figures S4A and S4B). Adaptive algorithms, such as least mean squares and recursive least squares, utilize a reference signal for movement cancellation.[35–38] Signals obtained either from a secondary IMU or from one of the orthogonal axes of the primary IMU fail to provide a reliable reference (Figures S4C–S4E). The challenge is that movements, especially those with small animals, can couple differently and in a nonstationary and noncorrelated manner at different parts of the body or in different directions at a single body location.[39]

A computation-based, self-adaptive approach for separating MA signals from cardiac activity and body movements effectively addresses this challenge (Figure 2A). The algorithm uses a high-order Savitzky-Golay polynomial smoothing filter (8th order and 21-point filter window) to fit slow variations in signal associated with movement-induced components of accelerations.[40,41] Subtraction of the smoothed content from the raw data leaves signals primarily associated with heart sounds. This scheme preserves high-order moments around inflection points, thereby retaining features such as local maxima and minima that are not retained through simple digital bandpass filters, via a least-squares polynomial fit around each point.[39,42] Comparisons of the same MA signal processed by bandpass filtering, wavelet denoising, and this Savitzky-Golay approach (Figure 2B, S4A, and S4B) demonstrate the effectiveness. Detailed, step-by-step results of the Savitzky-Golay approach illustrate clean, quasi-periodic cardiac cycles during both free movements of a CD1 mouse (Figure S4F) and when the mouse is at rest (Figure S4G).

Additional processing to extract the HR from these isolated cardiac sounds uses the Shannon energy envelope to generate smoothed signatures of cardiac cycles.[43,44] An automatic multi-scale-based peak detection (AMPD) algorithm identifies the heartbeats,[45] allowing determination of HR in each time window (1 s unless otherwise specified) from the mean beat-to-beat interval. Conventional approaches for determining the RR through

Please cite this article in press as: Ouyang et al., An implantable device for wireless monitoring of diverse physio-behavioral characteristics in freely behaving small animals and interacting groups, Neuron (2024), https://doi.org/10.1016/j.neuron.2024.02.020

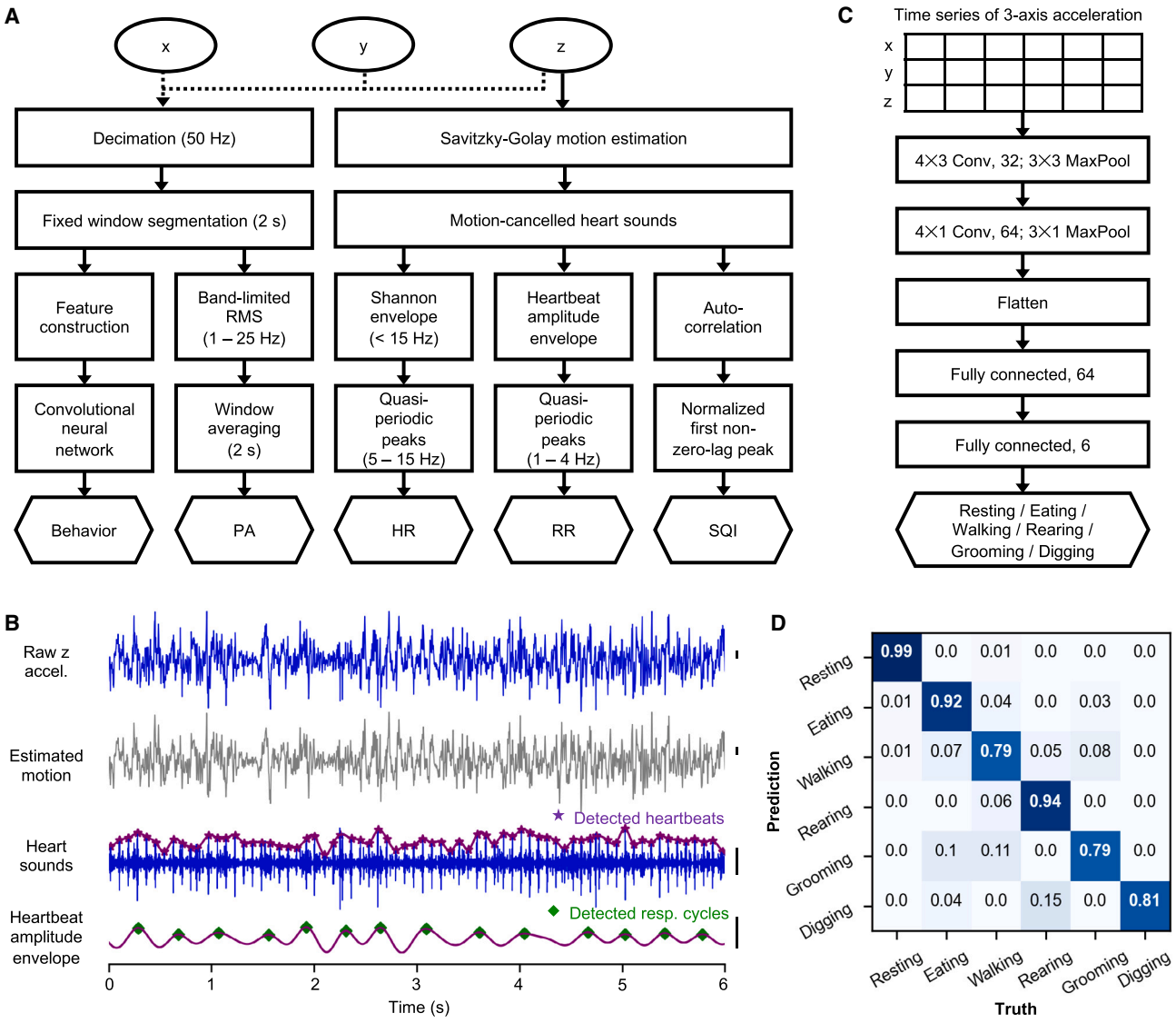

Figure 2. Flow diagrams and results from data analytics

(A) Flow diagram of the algorithms for quantifying physiology and behavior from mechano-acoustic (MA) data.

(B) Demonstration of the strategy for extracting physiological parameters from MA data. The scale bars represent 0.1 g.

(C) Architecture of the convolutional neural network (CNN) for classifying behavior based on MA data.

(D) Confusion matrix of the performance of this CNN.

accelerometry exploit the MA signal from chest wall expansion/contraction during respiration.[46,47] These approaches, however, are particularly sensitive to contributions to the signal from overall movements of the body, given their similar frequency content (~1 Hz). This study instead uses the modulation effect of respiration on the amplitude of heart-sound-related MA signals that follows from respiration-dependent variations of the distance between the heart and the accelerometer. This approach relies on heart sounds, thereby partially avoiding complications associated with movements. The envelope of the amplitude of extracted heart sounds, after bandpass filtering at 1–4 Hz (corresponding to the range of rodent RR: 60–240 breaths per minute [BrPM]), yields clearly distinguishable features associated with cycles of respiration (Figures 2B and S4F). More sophisticated algorithms, such as those utilizing the modulation effect of respiration on the amplitude ratio of S1 and S2 heart sounds, S1-S1 interval, or S1-S2 interval, may offer further elimination of movement-induced distortion of respiration signals.[26] The normalized first non-zero-lag peak of the autocorrelation of the extracted heart sound signal, a metric used to characterize the periodicity of a signal, serves as a signal quality index (SQI) that indicates the confidence of subsequently derived HR and RR. A high SQI corresponds to regularly spaced heartbeats.

Analysis of PA and behavioral states starts with decimation of the x, y, and z axis accelerations to 50 Hz, followed by fixed-window (2 s) segmentation of the signals for subsequent processing.

Please cite this article in press as: Ouyang et al., An implantable device for wireless monitoring of diverse physio-behavioral characteristics in freely behaving small animals and interacting groups, Neuron (2024), https://doi.org/10.1016/j.neuron.2024.02.020

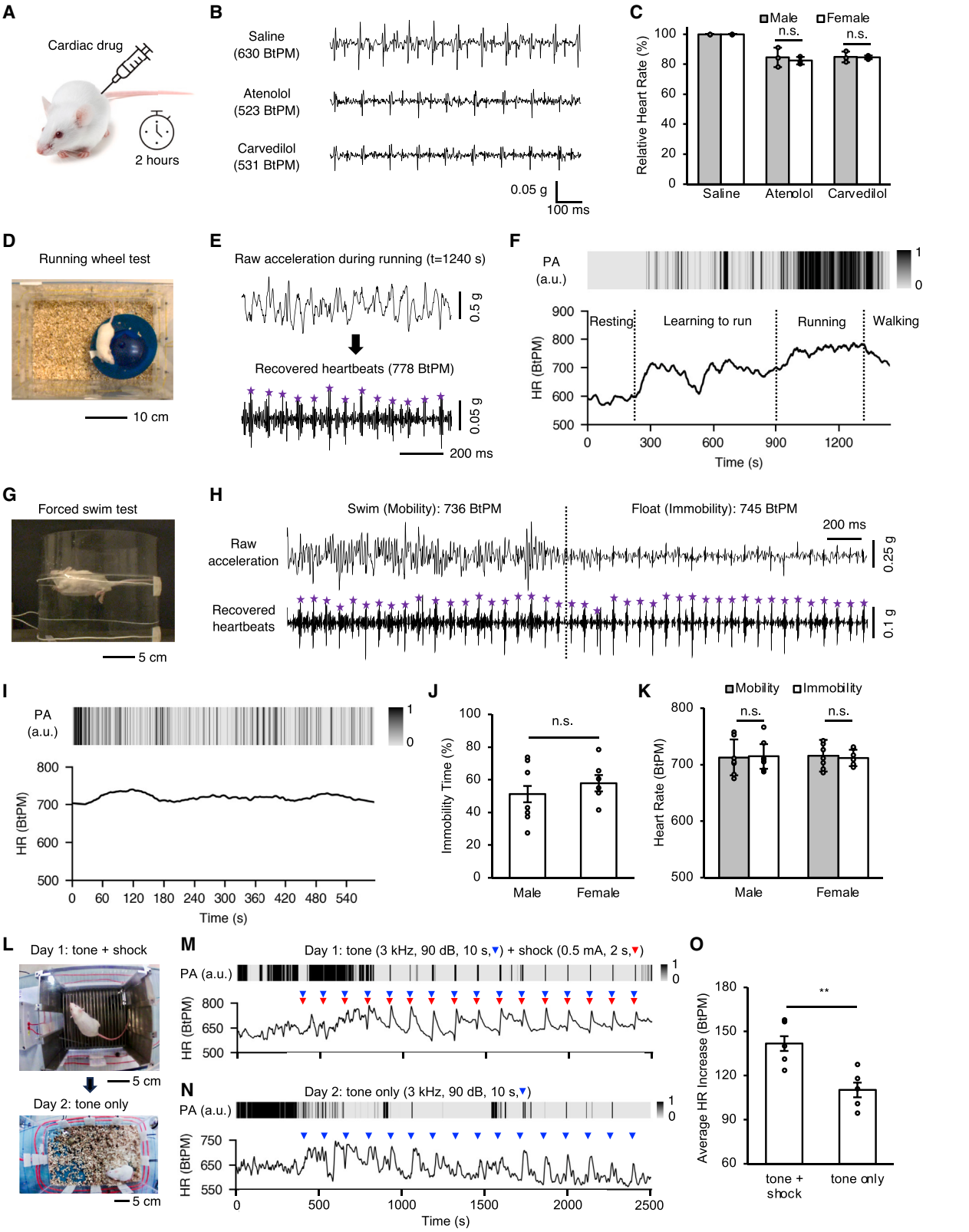

(legend on next page)

Please cite this article in press as: Ouyang et al., An implantable device for wireless monitoring of diverse physio-behavioral characteristics in freely behaving small animals and interacting groups, Neuron (2024), https://doi.org/10.1016/j.neuron.2024.02.020

The PA corresponds to the window average of the low-frequency, band-limited (1–25 Hz) root mean square (RMS) of 3 axis accelerations. The 3 axis accelerations of each window (2 s at 50 Hz), vertically stacked to a shape of 3 × 100, serve as the input feature for behavioral classification by a convolutional neural network (CNN), illustrated in Figure 2C and described in detail in the STAR Methods section. As shown in Figure S4H, MA signals of different behavioral states exhibit distinct temporal characteristics, thereby allowing for classification by machine learning approaches. The CNN model achieves a training accuracy of 0.92, a testing accuracy of 0.90, and precisions of 0.99, 0.92, 0.79, 0.94, 0.79, and 0.81, for resting, eating, walking, rearing, grooming, and digging, respectively (Figure 2D). Additional metrics in Table S2 indicate an average recall of 0.87 and an average F1 score of 0.87 for all behavioral classifications.

Validation of the accuracy of the MA data and its analysis involves comparison against two widely adopted technologies, MouseOx (Starr Life Sciences) and Eulerian video magnification (EVM).[48,49] MouseOx is a commercial pulse oximeter for measuring the HR, RR, and other physiological parameters in rodents via a tethered collar sensor. EVM is a computer vision-based algorithm that uses magnification of respiration-related movements of the chest wall for determination of the RR in resting animals. Comparison of results simultaneously measured by MA, MouseOx, and EVM in anesthetized and awake mice suggests that the device measures the HR and RR over a broad range of values and during movements with significantly higher accuracy and robustness than alternative technologies, as shown in detail in Figure S5.

Pharmacological, running wheel, forced swim, and shock grid tests

Unlike MouseOx and other tethered devices that restrict free movements and inhibit social interactions, the MA device does not alter the natural locomotor behavior of animals, nor does it induce anxiety-like behavior, as demonstrated with open-field testing (Figure S6). This feature creates opportunities for multiparametric physio-behavioral monitoring in neuroscience and biomedical research from unperturbed animal models. Here, we collectively demonstrate the broad applicability of the device under various experimental settings, including pharmacological, running wheel, forced swim, and shock grid tests.

The pharmacological test (Figure 3A) involves injection of atenolol and carvedilol, two beta-blocker drugs for treating hypertension, into MA-implanted male and female mice (n = 3/sex/drug). Representative z axis acceleration data collected 2 h post-injection (Figure 3B) indicate a reduction in HR from a baseline of 630 beats per minute (BtPM) to 523 and 531 BtPM after atenolol and carvedilol treatment, respectively. The amplitudes of MA signals from S1 and S2 heart sounds also decrease after treatment by either drug (Figure 3B), with a ~20 % decrease in mean relative HR (Figure 3C), where the p values against the baseline are all below 0.0001. The results reveal no significant difference between male and female mice ($p > 0.05$), consistent with known effects of the drugs.[50]

The running wheel test starts with placement of a wheel in a cage that houses a naive, implanted mouse in a resting state (Figure 3D). Representative z axis acceleration data show body movements in the raw data and clear cardiac cycles in the processed data during intense running activities (Figure 3E) as a demonstration of concurrent physio-behavioral monitoring, with time-dependent variations of HR and PA throughout the running wheel test (Figure 3F). After the placement of the wheel, the mouse exhibits an initial phase of learning to run, indicated by intermittent high-PA bouts, during which the HR varies with the intensity of the exercise in the range of ~600–725 BtPM. After about 10 min of exploration, the mouse enters a steady running state with high PA, during which the HR gradually increases from ~700 to ~780 BtPM. After about 7 min, the mouse stops running and starts walking in the cage, with its PA and HR gradually returning to the baseline. These data demonstrate opportunities for studying coordinated cardiac and physical activities in motor function research using the MA device.

The forced swim test is a standard assay for depression-like behavior by quantifying escape-related mobility of mice in an inescapable water tank.[51,52] Upon placement of a mouse in the tank (exposure to stress), the mouse attempts to escape by swimming (mobility) but also exhibits behavioral despair by floating (immobility). The percentage of mobility and immobility time provides a measure of depression-like behavior. Despite its wide usage for exploring brain changes associated with

Figure 3. Applications in physio-behavioral monitoring

(A) Schematic illustration of the cardiac drug test.
(B) Representative cardiac cycles (heart rate [HR]) after injection of saline, atenolol, and carvedilol.
(C) Variations of HR after injection of cardiac drugs. Data are represented as mean ± SEM.
(D) Photograph showing an implanted mouse on a running wheel.
(E) Representative acceleration data and recovered cardiac cycles during running.
(F) Integrated physio-behavioral monitoring (HR and physical activity [PA]) during running.
(G) Photograph showing an implanted mouse while swimming.
(H) Representative acceleration and recovered cardiac cycles in two consecutive bouts of swimming and floating.
(I) Integrated physio-behavioral monitoring during a forced swim test.
(J) Percentage of immobility time for male and female mice. Data are represented as mean ± SEM.
(K) HR of male and female mice in mobility and immobility states. Data are represented as mean ± SEM.
(L) Photographs showing a mouse being trained in a shock grid on day 1 by a predicting tone (3 kHz, 90 dB, 10 s), followed by an electrical shock (0.5 mA, 2 s), and being tested in its home cage on day 2 with only the predicting tone.
(M) The physio-behavioral responses of the mouse on day 1 when being presented with a series of tone + shock at an interval of 2 min and 15 s.
(N) The physio-behavioral responses of the mouse on day 2 when being presented with a series of tone only.
(O) The grand average of HR increase when being presented with 30 trials of tone + shock and tone only. Data are represented as mean ± SEM.

Please cite this article in press as: Ouyang et al., An implantable device for wireless monitoring of diverse physio-behavioral characteristics in freely behaving small animals and interacting groups, Neuron (2024), https://doi.org/10.1016/j.neuron.2024.02.020

stress and depression-like behaviors, the physiology behind these behaviors is not well known and is clearly a critical missing component in fully elucidating the underlying neural basis. Physio-behavioral monitoring provides important information in this context, which is challenging to capture using conventional tethered devices that restrict free swimming and/or are incompatible with aquatic environments. Studies with the experimental setup in Figure 3G yield z axis acceleration data (Figure 3H) that exhibit well-defined bouts of mobility and immobility, with expected features associated with body movements and cardiac activity. The analytics approach described previously recovers clear cardiac cycles even during periods of swimming (Figure 3H). The measured PA suggests that the animal frequently alternates between mobile and immobile states and that the HR does not change abruptly between these two states (Figure 3I). To quantify depression-like behavior, the PA data yield the time during the immobility state without the need for annotation of videos in standard methods. Corresponding results in Figure 3J indicate no significant differences in immobility time for male and female mice (n = 7/sex, $p > 0.05$). Statistical comparison of associated HRs in mobility and immobility states also suggests no significant differences (Figure 3K) for male and female mice ($p > 0.05$).

Data from the MA device can also offer insights into learning and cognition, as demonstrated in an associative learning task (Figure 3L). The test begins with a fear conditioning session on day 1 in a shock grid chamber, during which a mouse is presented with 30 tone-shock pairings that include a 10-s predicting tone (3 kHz, 95 dB) and a 2-s foot shock (0.5 mA) at the end of the tone. During this period, the mouse is in an initial active movement phase with high PA (Figure 3M). After the delivery of 4 tone-shock pairings, the animal demonstrates a freezing response (near zero PA) for the majority of the remainder of the session, a typical response to fear,[53] except for involuntary body shocks upon electrical stimulation. After the 4th delivery, each tone-shock pairing triggers an instantaneous increase of the HR, which decreases after the stimulation. The freezing behavior and rapid HR increase indicate learned association between tone and inescapable shock. On day 2 in its home chamber, the mouse is presented with 30 trials of tone (cue only) without trailing foot shocks. The mouse transitions from active movement (high PA) to mostly freezing (near zero PA) after the start of the tone-only trials (Figure 3N). Each tone delivery triggers an instantaneous increase of the HR, indicating fear associated with an anticipated shock. The grand average of the HR increases across the 30 trials show statistically significant differences between each condition (Figure 3O, n = 5 mice), consistent with different levels of fear with and without the foot shock.

Social interaction studies

MA sensing further reveals coordinated physio-behavioral responses to external stimuli in social interactions. In a resident-intruder test, the addition of a male intruder mouse (CD1) to the territory of a male resident mouse (CD1, implanted) elicits offensive and defensive behaviors.[54] A perforated, transparent partition across the middle of the test chamber allows for visual, olfactory, and auditory perception of the presence of the intruder (right chamber) by the resident (left chamber) without physical interaction (Figure 4A). MA signals show a pronounced increase in the HR of the resident from ~600 to ~750 BtPM within 3 min of introduction of the intruder into the partitioned side (Figure 4B). This increase precedes any behavioral change, as evidenced by the minimal increase in PA from the resting state during this period. The resident then actively confronts the isolated intruder by investigating the partition, with corresponding high values of PA. Upon removal of the partition, the resident launches physical attacks on the intruder, with further increases in HR up to ~790 BtPM. After removal of the intruder, the PA and HR of the resident gradually return to the resting state baseline within 30 min. As shown in Figure 4C, multiple independent trials (n = 3 male resident mice) suggest similar, phased, statistically significant increases in HR from baseline (587 ± 9 BtPM, mean ± SEM) to confrontation (728 ± 22 BtPM, mean ± SEM; $p < 0.05$) and from confrontation to attacking (777 ± 14 BtPM, mean ± SEM; $p < 0.05$).

To remove any interpretational or analytical confounds associated with direct physical contact, the witness defeat (also known as vicarious defeat) procedure allows for investigations of physio-behavioral responses under purely psychological stress.[55,56] This procedure uses a cage with a perforated, transparent partition in the middle. The left chamber houses the experimental witness mouse (CD1, MA implanted, male/female) that observes the interactions between a resident (CD1, male) mouse and a subordinate intruder (C57BL/6, male) mouse in the right chamber. The experimental witness mouse does not physically interact with the resident and intruder. The test includes the following five phases (Figure 4D): (1) witness only, (2) addition of the resident to the right chamber, (3) addition of the intruder to the right chamber, (4) removal of the intruder from the right chamber, and (5) removal of the resident from the right chamber. Figures 4E and 4F show representative dynamics of the HR and PA of male and female witnesses, respectively. The HRs of both male and female witnesses sharply increase upon observing the addition of the resident, followed by increases in their PAs. Next, after addition of the intruder, which subsequently triggers the attack from the resident, the HR of the male witness further increases (Figure 4E), suggesting that observing the fight increases its psychological arousal. By contrast, for the female witness, observing the fight does not alter a decreasing trend in HR (Figure 4F), as a reflection of no substantial increase of psychological arousal. These difference in responses for male and female (n = 4/sex) are statistically meaningful (Figure 4G, $p < 0.05$), consistent with sexual differences in the perception of stress.[57]

A final example in social behavioral studies demonstrates the use of the device in simultaneous recording from groups of freely interacting animals (n = 4, Figure 4H), a feature nearly impossible with tethered sensing devices and that is technically challenging using computer vision. The corresponding dynamics of PA (Figure 4I) and HR (Figure 4J) verify stable operation without interference among devices. As many as 13 devices can be operated in a single cage without compromised WPT performance.[58]

Chronic, continuous monitoring

The wireless power delivery mechanism and the biocompatible designs of these devices support capabilities for continuous,

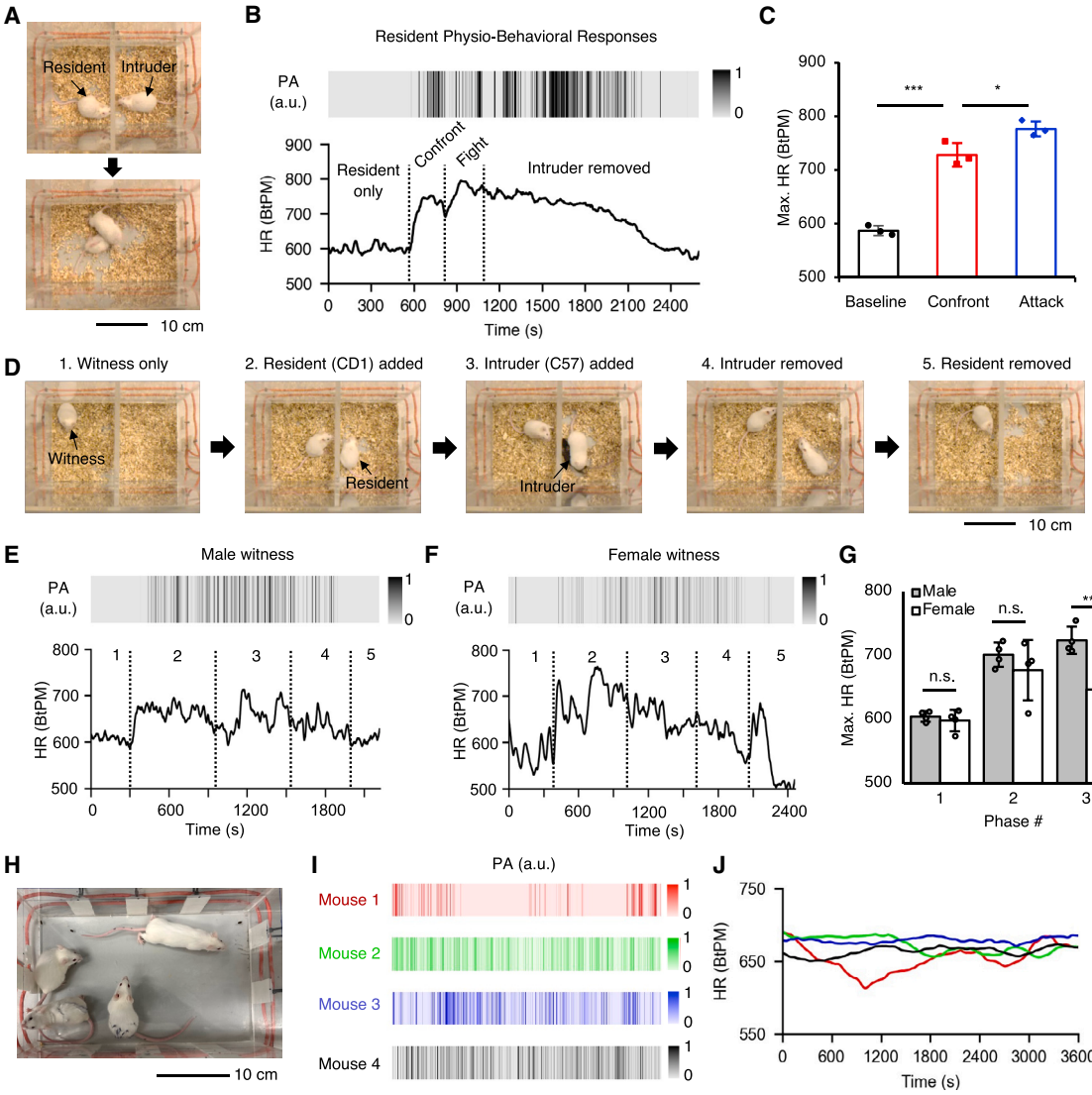

Figure 4. Applications in social interaction studies

(A) Photographs captured during an aggression study.
(B) Integrated physio-behavioral monitoring during the study.
(C) Variations of HR at different stages of the study.
(D) Photographs captured during a witness defeat test. Data are represented as mean ± SEM.
(E) Integrated physio-behavioral monitoring of a male witness during the test.
(F) Integrated physio-behavioral monitoring of a female witness during the test.
(G) Variations of HR at different phases of the test. Data are represented as mean ± SEM.
(H) Photograph of 4 freely interacting mice in the same cage while monitoring physio-behavioral data from each separately and continuously.
(I) Simultaneous monitoring of 4 freely interacting mice in the same cage.
(J) Corresponding HRs of the 4 mice during a 1-h period of monitoring.

long-term monitoring without time constraint, which is of relevance to chronic studies of both behavior and brain circuitry. Demonstration of this capability, in the context of circadian physiology, involves an implanted mouse fed *ad libitum* and under 12-h light/dark cycles for as long as experimental logistics allow (17 days in this case). Multiple physio-behavioral parameters over this period, extracted from MA and temperature data (Figure 5A), include subdermal temperature, HR, RR, and PA. The results exhibit clear circadian rhythms synchronous across different parameters. The temperature, HR, RR, and PA decrease during the light period (inactive phase) and increase during the dark period (active phase), in a rhythmic pattern over the 17 days. Figure 5B shows the behavioral states over one of the 24-h periods classified by MA signals, where the mouse is in a resting-dominated state during the light period and in a movement-dominated state during the dark period.

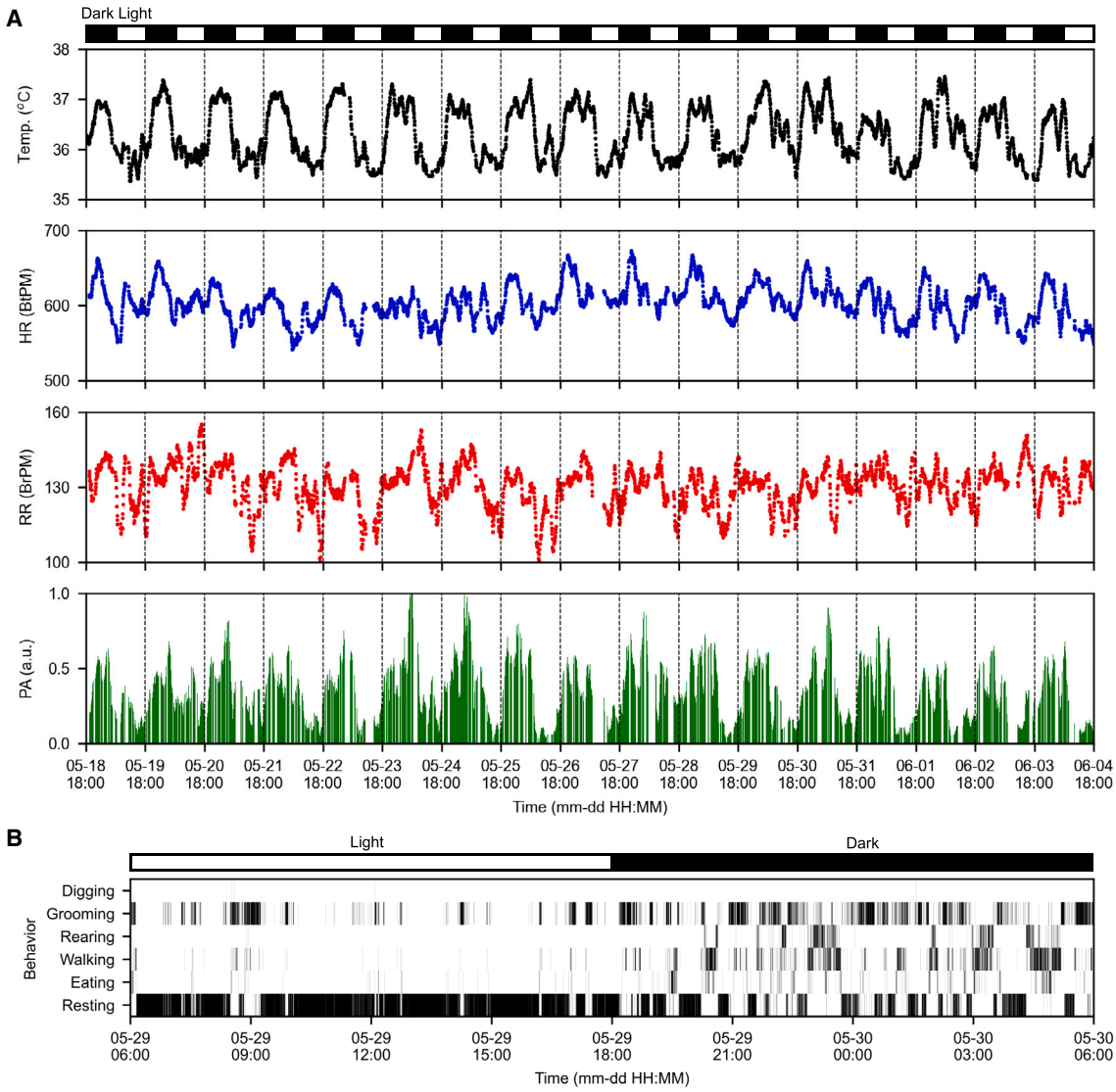

Figure 5. Chronic, continuous physio-behavioral monitoring (17 days) of a freely moving mouse

(A) Temperature (subdermal) and physio-behavioral (heart rate, respiratory rate, physical activity, and behavioral type) monitoring for a period of 17 consecutive days.

(B) Representative behavioral classification results during a 24-h period. The graph shows the behavioral state of each consecutive, non-overlapping window of 2 s during a 24-h period. This graph is a binary representation, where the occurrence of a behavioral state in a window of 2 s is indicated by a black-colored line and their non-occurrence is not colored.

Similar long-term studies can be conducted across any of the scenarios described previously.

Concurrent operation with wireless optogenetics

Being wireless and fully implantable, this device is compatible with a broad set of neuroscience research tools to enable sophisticated experimental paradigms. This work demonstrates its concurrent operation with a wireless, battery-free transcranial optogenetic device (NeuroLux, Figure 6A) for investigating the physio-behavioral characteristics upon optogenetic stimulation.[59] The optogenetic device uses pulsation of the NFC field for device programming (~10 s) via the standard NFC protocol and then delivers the defined stimulation (20 Hz, 2% duty cycle, 10 s) using a constant NFC field as the power source. The MA device operates stably during the pulsation of the NFC field thanks to the on-board supercapacitors that work as a transient source of power. The optogenetic device transcranially delivers red (628 nm) light to the right secondary motor cortex (M2) of C57BL/6 mice (Figures 6B and 6C) transduced with AAV1.Syn-ChrimsonR-tdT at least 4 weeks prior to device implantation. Figure 6D shows the CT image of a mouse implanted with both the optogenetic and MA devices. As previously reported, optogenetic stimulation of the M2 region induces significant rotational behavior (Figure 6E).[29,59] Continuous MA monitoring

Please cite this article in press as: Ouyang et al., An implantable device for wireless monitoring of diverse physio-behavioral characteristics in freely behaving small animals and interacting groups, Neuron (2024), https://doi.org/10.1016/j.neuron.2024.02.020

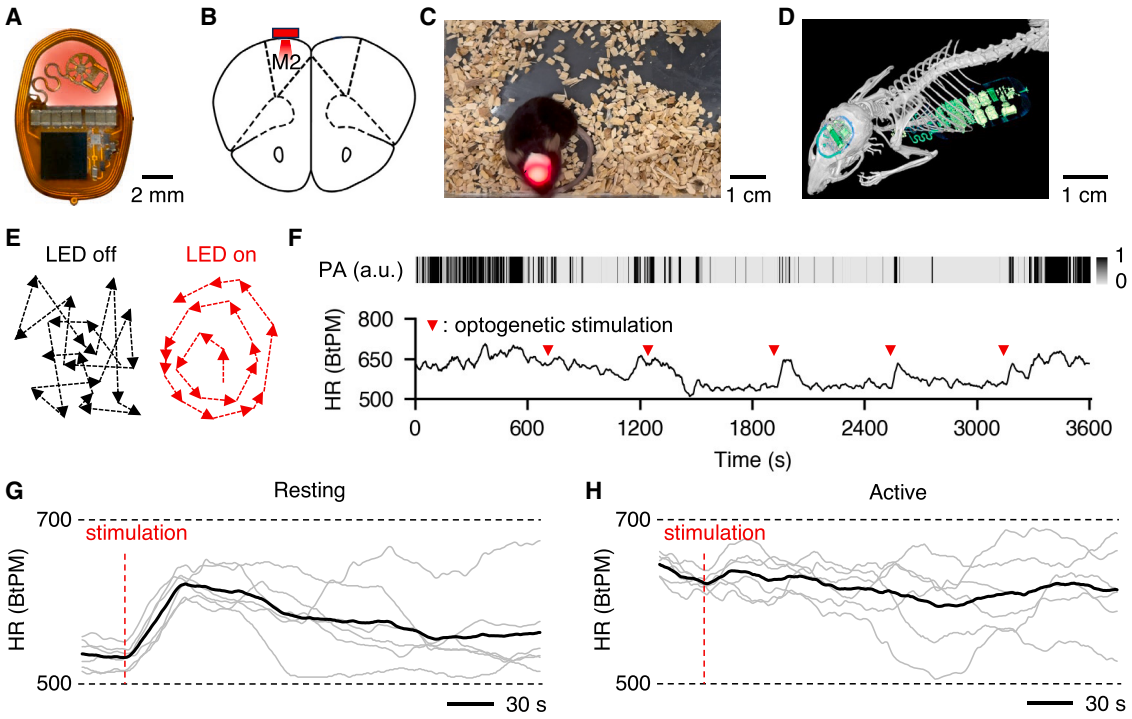

Figure 6. Concurrent operation with wireless optogenetics

(A) Photograph of a wireless, battery-free transcranial optogenetic device.

(B) Schematic illustration of transcranial optogenetic stimulation in M2 of a mouse transduced with AAV1.Syn-ChrimsonR-tdT.

(C) Photograph of an implanted mouse under optogenetic stimulation in a wireless power transfer cage.

(D) Micro-CT image of a mouse implanted with the optogenetic device and MA device.

(E) Example traces of an implanted mouse in a 20-s episode, with or without transcranial optogenetic stimulation.

(F) Physio-behavioral characteristics of a mouse under 5 consecutive optogenetic stimulations with 10-min intervals.

(G) Individual and average traces of HR variation across 6 trials upon optogenetic stimulation when the mouse was in an initial resting state.

(H) Individual and average traces of HR variation across 6 trials upon optogenetic stimulation when the mouse was in an initial active state.

(Figure 6F) suggests that the optogenetic stimulations elicit immediate increases of HR to different extents, depending on the state of the mouse. When the mouse is in an initial resting state (average PA < 0.001 a.u. in the 1-min pre-stimulation period), HR immediately increases from ~530 to ~620 BtPM in conjunction with rotational behavior and then gradually returns to the baseline as the animal resumes resting (Figure 6G). When the mouse is in an initial active state (average PA > 0.001 a.u. in the 1-min pre-stimulation period), HR slightly increases as the animal begins to rotate, but its peak value (~640 BtPM) does not appear to exceed the normal range of HR in the active state in the absence of stress factors (Figure 6H). It is evident from these results that the MA device may work coherently with other technologies to enable a wide range of neuroscience studies.

DISCUSSION

This report introduces advanced technology and data analytics approaches for integrated, multiparametric physio-behavioral monitoring in freely interacting small animal models, in wide-ranging scenarios of interest. The wireless, battery-free, soft, lightweight, miniature form factor of the fully implantable device allows for comprehensive measurements in minimally perturbed, naturally behaving mice across various settings, involving intense exercises, aquatic environments, and interacting groups, and including examples with simultaneous but independently controlled optogenetic neuromodulation. Specifically, the system yields real-time data with a full spectrum of MA signals associated with various physiological processes and behaviors, suitable for parsing by signal processing algorithms to yield multiple physiological (e.g., HR, RR, temperature, PA, etc.) and behavioral (e.g., eating, grooming, rearing, etc.) parameters. Future work combining 3 axis accelerometer and 3 axis gyroscope data, upon further optimization of WPT to stably power both the accelerometer and gyroscope, may offer a more comprehensive and accurate analysis of these physiological and behavioral parameters, as demonstrated by recent works on humans.[60–62] Such advances may expand the scope of monitored parameters to include gastrointestinal motility, musculoskeletal activity, hemodynamics, vocalization, and others. Integration of capabilities for neuromodulation represents an opportunity to both control and monitor neural activity. Beyond uses in neuroscience, the technology has utility in drug development, cardiovascular research, studies of disease models, biomarker discovery, and other areas that rely on freely moving, small animal models. Although WPT by resonant magnetic inductive coupling only

works efficiently within short distances (<1 m), this technology may still apply to large animals, for which batteries are a natural option. In this case, WPT remains valuable by facilitating wireless recharging of the batteries in a non-invasive manner during periods of minimal movement (e.g., sleep or restrained behavioral tasks).

STAR★METHODS

Detailed methods are provided in the online version of this paper and include the following:

- KEY RESOURCES TABLE
- RESOURCE AVAILABILITY
  - Lead contact
  - Materials availability
  - Data and code availability
- EXPERIMENTAL MODEL AND STUDY PARTICIPANT DETAILS
  - Animal subjects
- METHODS DETAILS
  - Electrical components
  - Assembly and encapsulation of the device
  - Finite element analysis
  - Wireless power transfer system
  - Characterization of wireless power transfer
  - Thermal characteristics
  - Surgical procedures
  - Microscale computed tomography imaging
  - Comparison against standard systems
  - Detailed signal processing algorithms
  - Open-field test and motion tracking
  - Pharmacological test
  - Running wheel test
  - Forced swim test
  - Shock grid test
  - Resident-intruder test
  - Witness defeat test
  - Chronic recording
  - Stereotactic injections
  - Transcranial device implantation
  - Optogenetic behavioral testing
- QUANTIFICATION AND STATISTICAL ANALYSIS

SUPPLEMENTAL INFORMATION

Supplemental information can be found online at https://doi.org/10.1016/j.neuron.2024.02.020.

ACKNOWLEDGMENTS

We acknowledge financial support from the Querrey Simpson Institute for Bioelectronics at Northwestern University and the National Institutes of Health (R43EB033239 and 1U01NS131406). This work made use of the NUFAB facility of Northwestern University's NUANCE Center, which has received support from the Soft and Hybrid Nanotechnology Experimental Resource (NSF ECCS1542205), the Materials Research Science and Engineering Center (DMR1720139), the State of Illinois, and Northwestern University. We acknowledge surgical and imaging work performed by the Developmental Therapeutics Core and the Center for Advanced Molecular Imaging at Northwestern University, which have received support from the Robert H Lurie Comprehensive Cancer Center (NCI CCSG 773 P30 CA060553). We acknowledge Alisha N. Spann for creating the CT images.

AUTHOR CONTRIBUTIONS

J.A.R., A.R.B., C.H.G., S.A.G., and W.O. conceived and supervised the project. W.O. developed the electronics, firmware, and algorithms. W.O. and J.T. developed the software. W.O., K.J.K., R.M.P.X., Y. Liu, Y. Lu, S.M.F., and Y.W. manufactured devices and characterized devices *in vitro* and *in vivo*. H. Luan conducted finite element analysis of the device. C.H.G., K.J.K., R.M.P.X., S.M.F., and M.W. developed device implantation procedures. C.H.G., K.J.K., R.M.P.X., S.M.F., M.W., S.A.G., M.H., K.M.P., E.M.H.-D., I.S., and N.G.-H. performed device implantation. C.H.G., K.J.K., R.M.P.X., S.M.F., W.O., M.W., J.A., I.J., H. Li, and Y.K. designed and conducted behavioral studies, chronic studies, and optogenetic studies. S.A.G., M.H., and K.M.P. designed and conducted device validation against MouseOx. W.O., C.H.G., and J.A.R. analyzed the data. C.R.H. designed and conducted CT imaging of implanted devices. W.O., J.A.R., C.H.G., and S.A.G. wrote the manuscript.

DECLARATION OF INTERESTS

J.A.R. and A.R.B. are co-founders of a company, NeuroLux Inc., that has potential commercial interest in this technology. C.H.G., K.J.K., R.M.P.X., S.M.F., J.A., and I.J. are employees of NeuroLux Inc.

Received: October 19, 2023
Revised: February 8, 2024
Accepted: February 28, 2024
Published: March 26, 2024

REFERENCES

1. LeDoux, J.E. (2000). Emotion circuits in the brain. Annu. Rev. Neurosci. *23*, 155–184.
2. Motta, S.C., Carobrez, A.P., and Canteras, N.S. (2017). The periaqueductal gray and primal emotional processing critical to influence complex defensive responses, fear learning and reward seeking. Neurosci. Biobehav. Rev. *76*, 39–47.
3. Signoret-Genest, J., Schukraft, N., L Reis, S., Segebarth, D., Deisseroth, K., and Tovote, P. (2023). Integrated cardio-behavioral responses to threat define defensive states. Nat. Neurosci. *26*, 447–457.
4. Walker, P., and Carrive, P. (2003). Role of ventrolateral periaqueductal gray neurons in the behavioral and cardiovascular responses to contextual conditioned fear and poststress recovery. Neuroscience *116*, 897–912.
5. Libanori, A., Chen, G., Zhao, X., Zhou, Y., and Chen, J. (2022). Smart textiles for personalized healthcare. Nat. Electron. *5*, 142–156.
6. Won, S.M., Cai, L., Gutruf, P., and Rogers, J.A. (2023). Wireless and battery-free technologies for neuroengineering. Nat. Biomed. Eng. *7*, 405–423.
7. Hong, Y.J., Jeong, H., Cho, K.W., Lu, N., and Kim, D. (2019). Wearable and implantable devices for cardiovascular healthcare: from monitoring to therapy based on flexible and stretchable electronics. Adv. Funct. Mater. *29*, 1808247.
8. Schonle, P., Wang, Q., Brun, N., Bosser, J., Meier, P., and Huang, Q. (2017). Towards an implantable telemetry system for SpO_2 and PWV measurement in small animals. In IEEE Biomedical Circuits and Systems Conference (BioCAS) (IEEE), pp. 1–4.
9. Wang, Q., Brun, N., Huang, Q., and Schönle, P. (2018). A10383 Towards an Implantable Telemetry System for Photoplethysmography Based Vital Signs Monitoring in Small Animals. J. Hypertens. *36*, e12.
10. Ausra, J., Madrid, M., Yin, R.T., Hanna, J., Arnott, S., Brennan, J.A., Peralta, R., Clausen, D., Bakall, J.A., Efimov, I.R., et al. (2022). Wireless,

fully implantable cardiac stimulation and recording with on-device computation for closed-loop pacing and defibrillation. Sci. Adv. *8*, eabq7469.

11. Russell, D.M., McCormick, D., Taberner, A.J., Malpas, S.C., and Budgett, D.M. (2011). A high bandwidth fully implantable mouse telemetry system for chronic ECG measurement. In 2011 Annual International Conference of the IEEE Engineering in Medicine and Biology Society (IEEE), pp. 7666–7669.
12. Ouyang, W., Lu, W., Zhang, Y., Liu, Y., Kim, J.U., Shen, H., Wu, Y., Luan, H., Kilner, K., Lee, S.P., et al. (2023). A wireless and battery-less implant for multimodal closed-loop neuromodulation in small animals. Nat. Biomed. Eng. *7*, 1252–1269.
13. Mathis, M.W., and Mathis, A. (2020). Deep learning tools for the measurement of animal behavior in neuroscience. Curr. Opin. Neurobiol. *60*, 1–11.
14. Nilsson, S.R.O., Goodwin, N.L., Choong, J.J., Hwang, S., Wright, H.R., Norville, Z.C., Tong, X., Lin, D., Bentzley, B.S., and Eshel, N. (2020). Simple Behavioral Analysis (SimBA)–an open source toolkit for computer classification of complex social behaviors in experimental animals. Preprint at bioRxiv.
15. Topalovic, U., Aghajan, Z.M., Villaroman, D., Hiller, S., Christov-Moore, L., Wishard, T.J., Stangl, M., Hasulak, N.R., Inman, C.S., Fields, T.A., et al. (2020). Wireless programmable recording and stimulation of deep brain activity in freely moving humans. Neuron *108*, 322–334.e9.
16. Dagher, S., and Ishiyama, S. (2023). Protocol for precise signal synchronization of electrophysiology, videography, and audio recordings using a custom-made pulse generator. Star Protoc. *4*, 102306.
17. Lee, K.H., Ni, X., Lee, J.Y., Arafa, H., Pe, D.J., Xu, S., Avila, R., Irie, M., Lee, J.H., Easterlin, R.L., et al. (2020). Mechano-acoustic sensing of physiological processes and body motions via a soft wireless device placed at the suprasternal notch. Nat. Biomed. Eng. *4*, 148–158.
18. Panda, B., Mandal, S., and Majerus, S.J.A. (2019). Flexible, skin coupled microphone array for point of care vascular access monitoring. IEEE Trans. Biomed. Circuits Syst. *13*, 1494–1505.
19. Laulicht, B., Tripathi, A., Schlageter, V., Kucera, P., and Mathiowitz, E. (2010). Understanding gastric forces calculated from high-resolution pill tracking. Proc. Natl. Acad. Sci. USA *107*, 8201–8206.
20. Jeong, H., Yoo, J.Y., Ouyang, W., Greane, A.L.J.X., Wiebe, A.J., Huang, I., Lee, Y.J., Lee, J.Y., Kim, J., Ni, X., et al. (2023). Closed-loop network of skin-interfaced wireless devices for quantifying vocal fatigue and providing user feedback. Proc. Natl. Acad. Sci. USA *120*, e2219394120.
21. Ni, X., Ouyang, W., Jeong, H., Kim, J.T., Tzaveils, A., Mirzazadeh, A., Wu, C., Lee, J.Y., Keller, M., Mummidisetty, C.K., et al. (2021). Automated, multiparametric monitoring of respiratory biomarkers and vital signs in clinical and home settings for COVID-19 patients. Proc. Natl. Acad. Sci. USA *118*, e2026610118.
22. Jeong, H., Kwak, S.S., Sohn, S., Lee, J.Y., Lee, Y.J., O'Brien, M.K., Park, Y., Avila, R., Kim, J.T., Yoo, J.Y., et al. (2021). Miniaturized wireless, skin-integrated sensor networks for quantifying full-body movement behaviors and vital signs in infants. Proc. Natl. Acad. Sci. USA *118*, e2104925118.
23. Pasquet, M.O., Tihy, M., Gourgeon, A., Pompili, M.N., Godsil, B.P., Léna, C., and Dugué, G.P. (2016). Wireless inertial measurement of head kinematics in freely-moving rats. Sci. Rep. *6*, 35689.
24. Shih, Y.H., and Young, M.S. (2007). Integrated digital image and accelerometer measurements of rat locomotor and vibratory behaviour. J. Neurosci. Methods *166*, 81–88.
25. Venkatraman, S., Jin, X., Costa, R.M., and Carmena, J.M. (2010). Investigating neural correlates of behavior in freely behaving rodents using inertial sensors. J. Neurophysiol. *104*, 569–575.
26. Pandia, K., Inan, O.T., Kovacs, G.T.A., and Giovangrandi, L. (2012). Extracting respiratory information from seismocardiogram signals acquired on the chest using a miniature accelerometer. Physiol. Meas. *33*, 1643–1660.
27. Kim, B.J., and Meng, E. (2016). Micromachining of Parylene C for bioMEMS. Polym. Adv. Technol. *27*, 564–576.
28. Poojari, Y. (2017). Silicones for encapsulation of medical device implants. Silicon *9*, 645–649.
29. Yang, Y., Wu, M., Vázquez-Guardado, A., Wegener, A.J., Grajales-Reyes, J.G., Deng, Y., Wang, T., Avila, R., Moreno, J.A., Minkowicz, S., et al. (2021). Wireless multilateral devices for optogenetic studies of individual and social behaviors. Nat. Neurosci. *24*, 1035–1045.
30. Mickle, A.D., Won, S.M., Noh, K.N., Yoon, J., Meacham, K.W., Xue, Y., McIlvried, L.A., Copits, B.A., Samineni, V.K., Crawford, K.E., et al. (2019). A wireless closed-loop system for optogenetic peripheral neuromodulation. Nature *565*, 361–365.
31. Madhvapathy, S.R., Wang, J.J., Wang, H., Patel, M., Chang, A., Zheng, X., Huang, Y., Zhang, Z.J., Gallon, L., and Rogers, J.A. (2023). Implantable bioelectronic systems for early detection of kidney transplant rejection. Science *381*, 1105–1112.
32. Reichert, W.M. (2007). Indwelling Neural Implants: Strategies for Contending with the In Vivo Environment (CRC Press).
33. Allen, J. (2007). Photoplethysmography and its application in clinical physiological measurement. Physiol. Meas. *28*, R1–R39.
34. Messer, S.R., Agzarian, J., and Abbott, D. (2001). Optimal wavelet denoising for phonocardiograms. Microelectron. J. *32*, 931–941.
35. Bhotto, M.Z.A., and Antoniou, A. (2012). New improved recursive least-squares adaptive-filtering algorithms. IEEE Trans. Circuits Syst. I *60*, 1548–1558.
36. Eksioglu, E.M. (2011). Sparsity regularised recursive least squares adaptive filtering. IET Signal Process. *5*, 480–487.
37. Poularikas, A.D. (2017). Adaptive Filtering: Fundamentals of Least Mean Squares with MATLAB® (CRC Press).
38. Biswas, U., Das, A., Debnath, S., and Oishee, I. (2014). ECG signal denoising by using least-mean-square and normalised-least-mean-square algorithm based adaptive filter. In 2014 International Conference on Informatics, Electronics & Vision (ICIEV) (IEEE), pp. 1–6.
39. Pandia, K., Ravindran, S., Cole, R., Kovacs, G., and Giovangrandi, L. (2010). Motion artifact cancellation to obtain heart sounds from a single chest-worn accelerometer. In 2010 IEEE International Conference on Acoustics, Speech and Signal Processing (IEEE), pp. 590–593.
40. Schafer, R.W. (2011). What is a Savitzky-Golay filter? [lecture notes]. IEEE Signal Process. Mag. *28*, 111–117.
41. Press, W.H., and Teukolsky, S.A. (1990). Savitzky-Golay smoothing filters. Comput. Phys. *4*, 669–672.
42. Press, W.H., Teukolsky, S.A., Vetterling, W.T., and Flannery, B.P. (2007). Numerical Recipes: The Art of Scientific Computing, Third Edition (Cambridge University Press).
43. Zhu, H., and Dong, J. (2013). An R-peak detection method based on peaks of Shannon energy envelope. Biomed. Signal Process. Control *8*, 466–474.
44. Park, J.S., Lee, S.W., and Park, U. (2017). R peak detection method using wavelet transform and modified shannon energy envelope. J. Healthc. Eng. *2017*, 4901017.
45. Scholkmann, F., Boss, J., and Wolf, M. (2012). An efficient algorithm for automatic peak detection in noisy periodic and quasi-periodic signals. Algorithms *5*, 588–603.
46. Bates, A., Ling, M.J., Mann, J., and Arvind, D.K. (2010). Respiratory rate and flow waveform estimation from tri-axial accelerometer data. In 2010 International Conference on Body Sensor Networks (IEEE), pp. 144–150.
47. Hung, P.D., Bonnet, S., Guillemaud, R., Castelli, E., and Yen, P.T.N. (2008). Estimation of respiratory waveform using an accelerometer. In 2008 5th IEEE International Symposium on Biomedical Imaging: From Nano to Macro (IEEE), pp. 1493–1496.
48. Wadhwa, N., Wu, H.-Y., Davis, A., Rubinstein, M., Shih, E., Mysore, G.J., Chen, J.G., Buyukozturk, O., Guttag, J.V., Freeman, W.T., et al. (2016). Eulerian video magnification and analysis. Commun. ACM *60*, 87–95.

49. Wu, H.-Y., Rubinstein, M., Shih, E., Guttag, J., Durand, F., and Freeman, W. (2012). Eulerian video magnification for revealing subtle changes in the world. ACM Trans. Graphics *31*, 1–8.

50. Schaefer, W.H., Politowski, J., Hwang, B., Dixon, F., Goalwin, A., Gutzait, L., Anderson, K., DeBrosse, C., Bean, M., and Rhodes, G.R. (1998). Metabolism of carvedilol in dogs, rats, and mice. Drug Metab. Dispos. *26*, 958–969.

51. Can, A., Dao, D.T., Arad, M., Terrillion, C.E., Piantadosi, S.C., and Gould, T.D. (2012). The mouse forced swim test. J. Vis. Exp. e3638.

52. Yankelevitch-Yahav, R., Franko, M., Huly, A., and Doron, R. (2015). The forced swim test as a model of depressive-like behavior. J. Vis. Exp. 52587.

53. Buccafusco, J.J. (2000). Methods of Behavior Analysis in Neuroscience (CRC Press).

54. Koolhaas, J.M., Coppens, C.M., de Boer, S.F., Buwalda, B., Meerlo, P., and Timmermans, P.J.A. (2013). The resident-intruder paradigm: a standardized test for aggression, violence and social stress. J. Vis. Exp. 4367.

55. Warren, B.L., Mazei-Robison, M.S., Robison, A.J., and Iñiguez, S.D. (2020). Can I get a witness? Using vicarious defeat stress to study mood-related illnesses in traditionally understudied populations. Biol. Psychiatry *88*, 381–391.

56. Iñiguez, S.D., Flores-Ramirez, F.J., Riggs, L.M., Alipio, J.B., Garcia-Carachure, I., Hernandez, M.A., Sanchez, D.O., Lobo, M.K., Serrano, P.A., Braren, S.H., et al. (2018). Vicarious social defeat stress induces depression-related outcomes in female mice. Biol. Psychiatry *83*, 9–17.

57. Palanza, P., and Parmigiani, S. (2017). How does sex matter? Behavior, stress and animal models of neurobehavioral disorders. Neurosci. Biobehav. Rev. *76*, 134–143.

58. Shin, G., Gomez, A.M., Al-Hasani, R., Jeong, Y.R., Kim, J., Xie, Z., Banks, A., Lee, S.M., Han, S.Y., Yoo, C.J., et al. (2017). Flexible near-field wireless optoelectronics as subdermal implants for broad applications in optogenetics. Neuron *93*, 509–521.e3.

59. Ausra, J., Wu, M., Zhang, X., Vázquez-Guardado, A., Skelton, P., Peralta, R., Avila, R., Murickan, T., Haney, C.R., Huang, Y., et al. (2021). Wireless, battery-free, subdermally implantable platforms for transcranial and long-range optogenetics in freely moving animals. Proc. Natl. Acad. Sci. USA *118*, e2025775118.

60. Pärkkä, J., Ermes, M., Antila, K., Van Gils, M., Mänttäri, A., and Nieminen, H. (2007). Estimating intensity of physical activity: a comparison of wearable accelerometer and gyro sensors and 3 sensor locations. In 2007 29th Annual International Conference of the IEEE Engineering in Medicine and Biology Society (IEEE), pp. 1511–1514.

61. Lahdenoja, O., Hurnanen, T., Jafari Tadi, M.J., Pänkäälä, M., and Koivisto, T. (2016). Heart rate variability estimation with joint accelerometer and gyroscope sensing. In 2016 Computing in Cardiology Conference (CinC) (IEEE), pp. 717–720.

62. Yang, C., and Tavassolian, N. (2018). Combined seismo-and gyro-cardiography: A more comprehensive evaluation of heart-induced chest vibrations. IEEE J. Biomed. Health Inform. *22*, 1466–1475.

63. Klapoetke, N.C., Murata, Y., Kim, S.S., Pulver, S.R., Birdsey-Benson, A., Cho, Y.K., Morimoto, T.K., Chuong, A.S., Carpenter, E.J., Tian, Z., et al. (2014). Independent optical excitation of distinct neural populations. Nat. Methods *11*, 338–346.

64. Mathis, A., Mamidanna, P., Cury, K.M., Abe, T., Murthy, V.N., Mathis, M.W., and Bethge, M. (2018). DeepLabCut: markerless pose estimation of user-defined body parts with deep learning. Nat. Neurosci. *21*, 1281–1289.

65. Doloff, J.C., Veiseh, O., de Mezerville, R., Sforza, M., Perry, T.A., Haupt, J., Jamiel, M., Chambers, C., Nash, A., Aghlara-Fotovat, S., et al. (2021). The surface topography of silicone breast implants mediates the foreign body response in mice, rabbits and humans. Nat. Biomed. Eng. *5*, 1115–1130.

Please cite this article in press as: Ouyang et al., An implantable device for wireless monitoring of diverse physio-behavioral characteristics in freely behaving small animals and interacting groups, Neuron (2024), https://doi.org/10.1016/j.neuron.2024.02.020

STAR★METHODS

KEY RESOURCES TABLE

REAGENT or RESOURCE	SOURCE	IDENTIFIER
Chemicals, peptides, and recombinant proteins		
Atenolol	MilliporeSigma	PHR1909
Carvedilol	MilliporeSigma	PHR1265
Bacterial and virus strains		
AAV1.Syn-ChrimsonR-tdT	Klapoetke et al.[63] Dr. Edward Boyden	Addgene viral prep #59171-AAV1
Experimental models: Organisms/strains		
CD1 mice	Charles River Laboratories	Strain Code: 022
C57BL/6 mice	Charles River Laboratories	Strain Code: 027
Sprague Dawley rat	Charles River Laboratories	Strain Code: 001
Software and algorithms		
Python 3.8.10	Python Software Foundation	https://www.python.org
Scipy 1.7.3	Scipy Project Team	https://scipy.org
Numpy 1.20.2	Numpy Project Team	https://numpy.org
Pandas 1.2.5	Pandas Project Team	https://pandas.pydata.org
Matplotlib 3.3.4	Matplotlib Project Team	https://matplotlib.org
Tensorflow 2.4	Google	https://www.tensorflow.org
DeepLabCut 2.2.1	Mathis et al.[64] the A. and M.W. Mathis Labs	https://github.com/DeepLabCut/DeepLabCut

RESOURCE AVAILABILITY

Lead contact

Further information and requests for resources should be directed to and will be fulfilled by the lead contact, Dr. John A. Rogers (jrogers@northwestern.edu).

Materials availability

This study did not generate new unique reagents.

Data and code availability

All data reported in this paper will be shared by the lead contact upon request. The original code for signal processing is available at: https://doi.org/10.7910/DVN/9PQL0F.

EXPERIMENTAL MODEL AND STUDY PARTICIPANT DETAILS

Animal subjects

All experiments used adult CD1 mice (40-45 g at start of experiments), C57BL/6 mice (25-35 g at start of experiments) and adult Sprague Dawley rats (250–350 g at start of experiments) from Charles River Laboratories (Wilmington, MA), maintained on a 12-hr light/dark cycle and fed ad libitum. All experimental procedures were conducted in accordance with the National Institutes of Health standards and were approved by the Institutional Animal Care and Use Committee (IACUC) at Northwestern University or the University of Washington, Seattle.

METHODS DETAILS

Electrical components

The system was assembled on a double-layer fPCB [Cu (18 μm): Polyimide (PI, 75 μm): Cu (18 μm)]. A receiver coil (10 turns, trace width/space of 100 μm/100 μm, area of 10 mm × 24 mm) on the fPCB paired with two tuning capacitors (1 – 100 pF) yielded a

resonant peak at 13.56 MHz for WPT. High-speed Schottky diodes in a full-wave bridge rectifier followed by a first-order RC filter converted the inductively coupled AC voltage to a DC voltage. An LDO linear voltage regulator (ADP7112, Analog Devices Inc.) in 6-pin wafer-level chip-scale package (WLCSP) (1.2 mm × 1 mm) converted the DC voltage to a constant voltage supply (2.5 V) to power the system. An array of 4 supercapacitors (CPX3225A752D, Seiko Instruments) that connected to the output of the voltage regulator provided a temporary power source in the event of compromised WPT. A BLE SoC (nRF52832-CIAA, Nordic Semiconductor, Norway) in WLCSP packaging (3.0 mm × 3.2 mm) served as the CPU and Bluetooth communication module. A low-power inertial measurement unit (BMI160, Bosch Sensortec, Germany) with a footprint of 2.5 mm × 3.0 mm served as the accelerometer and gyroscope and connected to the BLE SoC via the SPI interface. An ultra-low-power (25 μW) temperature sensor (MAX31875, Maxim Integrated Inc.) in WLCSP packaging (0.84 mm × 0.84 mm) measured the subdermal temperature. The BLE SoC used a miniaturized (3.2 mm × 1.6 mm) ceramic 2.45 GHz antenna (2450AT18A100, Johanson Technology Inc.) for wireless communication. Use of other passive components with 0201 (imperial) packaging minimized the overall size of the system.

Assembly and encapsulation of the device

Following hot-air soldering of electrical components to the fPCB, application of an epoxy adhesive (Loctite 3621, Henkel, Rocky Hill, CT) to the BLE SoC and BMI160 followed by curing at 95 °C for 25 min provided mechanical protection for the chips. Chemical vapor deposition formed conformal coatings of Parylene-C (30 μm) to encapsulate the device. Spin coating of PDMS (Sylgard 184, 10:1) on a plastic substrate at 300 rpm for 1 min followed by curing at 95 °C for 10 min formed the base encapsulation layer. Spin coating of PDMS on the base layer at 500 rpm for 1 min formed an uncured layer of PDMS. Gently pressing the Parylene-coated device into the uncured PDMS followed by curing at 95 °C for 10 min formed the PDMS encapsulation layer. Subsequent drop casting of uncured PDMS onto electrical components followed by curing at 95 °C for 10 min ensured full coverage of the components. The final thickness of the encapsulated device is 3 mm.

Finite element analysis

2D dynamic finite element analysis performed in the commercial software suite Abaqus examined the dynamic responses of the accelerometer within the implantable devices with different geometric designs and/or encapsulation strategies. Four-node shell elements were chosen for the accelerometer, encapsulation, and tissue/skin, with fine mesh near the accelerometer. The implicit solver was used. No energy dissipation was considered in the model. The accelerometer was simplified as molding compound, a linear elastic material characterized by elastic modulus of 25 GPa, Poisson's ratio of 0.3, and density of 1.78 g/cm^3. The PDMS encapsulation and the tissue/skin were modeled as incompressible elastomeric materials with Mooney-Rivlin hyperelastic behavior. PDMS (Sylgard 184, 10:1) was characterized by elastic modulus of 1.8 MPa and density of 0.965 g/cm^3. Tissue and skin were simplified with elastic modulus of 300 kPa and density of 1.0 g/cm^3.

Wireless power transfer system

The full system setup included a power distribution control (PDC) box, an antenna impedance matching box, a laptop for controlling the output power level of the PDC box, a cage wired with a double-loop primary antenna (rat cage, 34 cm × 31 cm × 30 cm; mouse cage, 30 cm × 20 cm × 20 cm), and a tablet with a custom application for recording data and issuing commands wirelessly.

Characterization of wireless power transfer

The test used a device assembled only with WPT components and with the LDO regulator connected to a potentiometer inside a cage encircled by a double-loop primary antenna. Decreasing the resistance of the potentiometer to a value R_0 below which the LDO was unable to provide a fixed output voltage identified the point at which the LDO no longer dissipated power by heating. Calculation of the capability for WPT used the following equation:

$$P = \frac{{V_0}^2}{R_0}$$

Performing this measurement with the device at different positions inside the cage defined the distribution of wirelessly transferred power. A custom Python script enabled 2D interpolation of the results. Mounting this device on the back of an adult rat/mouse model made of agarose gel placed at different angles simulated the rearing behavior and other normal activities. Performing this measurement and recording the device operating time after oriented it to different rearing angles for locations at the center and corner of the cage quantified the effects on WPT.

Thermal characteristics

An infrared imaging camera (TG165, Teledyne FLIR LLC) characterized the heating of the device in air when powered by WPT at the center and corner of a mouse cage. The testing setup for characterizing the temperature sensing accuracy involved a fully encapsulated device and a commercial thermocouple (HH374, Omega Engineering Inc.) in the vicinity, which were submerged in a water bath. The device and the thermocouple data logger recorded the temperature simultaneously as the water bath naturally cooled from 40 °C.

Surgical procedures

All procedures complied with Animal Welfare and IACUC policies under approved protocols using aseptic conditions. The animal was anesthetized in an induction chamber (2-3 % isoflurane, mice; 4-5 % isoflurane, rats). Once anesthetized, the animal's abdomen was shaved before placing it in a supine position above a regulated heating pad in a stereotaxic frame (Kopf; Figure S1A). The animal was maintained at a surgical plane of anesthesia using 1–3 % isoflurane for the duration of surgery. Meloxicam (20 mg kg−1, mice; 2 mg kg−1, rats; subcutaneous injection) and bupivacaine (2 mg kg−1, intradermal injection [both species]) worked as preoperative analgesics. After the animal reached a stable plane of anesthesia, a marker was used to denote the skin area directly above the animal's heart. An ∼10 mm, horizontal incision was made on the ventral side of the animal midway across body of the device (Figure S1A). This prevents the edge of the device from irritating the wound once implanted. Blunt forceps were used to separate the subcutaneous fascia in both the anterior and posterior directions, creating a pocket for the device. The device was manually inserted into the anterior portion of the incision. The skin was then manipulated around the device until the sensor was located directly underneath the marked area indicating the location of the heart. A small amount of tissue adhesive (GLUture) was then applied between the device body and the underlying muscle followed by a smaller amount of adhesive applied between the sensor and the underlying muscle. Finally, three 7 mm wound clips were used to close the incision. The animal was allowed to recover for ∼30 minutes before transfer to the cage area facility for further monitoring. A second dose of Meloxicam (20 mg kg−1, mice; 2 mg kg−1, rats; subcutaneous injection) was administered 24 hours after initial recovery for extended analgesia. After 5 days, the animal was lightly anesthetized and the wound clips were removed. Device testing occurred after the removal of the wound clips and surgical recovery.

This surgical procedure was amended to accommodate both sexes in both species (rats and mice). The original surgical procedure called for two incisions, one across the device body (as performed now) and the other above the IMU pad for ease and accuracy of placement above the heart. The second incision across the IMU pad greatly irritated female animals, as these incisions were made near or on their mammary glands.[65] The updated single incision method strategically places the incision between the female mammary glands, thus eliminating their discomfort and scratching at the implanted devices.

Microscale computed tomography imaging

X-ray computed tomography (CT) imaging was performed with a preclinical microCT imaging system (nanoScan PET/CT, Mediso-USA, Arlington VA). Mouse data were acquired with 'Medium' zoom, 1x1 binning, with 720 projection views over a full circle, using 70 kVp/980 μA, with a 90 ms exposure time. Rat data were acquired with 'Maximum FOV' zoom, 1x4 binning, with 1440 projection views over two full rotations, using 70 kVp/980 μA, with a 90 ms exposure time. Reconstruction of mouse and rat data used a voxel size of 34 μm and 125 μm, respectively, with filtered (Butterworth filter) back-projection software from Mediso Nucline (version 3.04.018). The reconstructed data was visualized and segmented in Amira 2022.1 (FEI Company, Thermo-Fisher, Hillsboro, OR). A non-local-means filter was used to reduce image artifacts.

Comparison against standard systems

A MouseOx pulse oximeter was used to measure the HR and RR of a mouse through a wired, collar sensor clamped to the neck. A cage wired with a double-loop primary antenna housed a mouse implanted with the MA device and tethered to the collar sensor. For the comparison under anesthesia, isoflurane was supplied via a nose cone. The isoflurane concentration varied at the following sequence: 0.5 %, 1.0 %, 1.5 %, 2.0 %, 1.5 %, 1.0 %, 0.5 %. Each isoflurane concentration lasted for 5 min. An overhead camera (acA1920-25gc, Basler AG, Germany) recorded the experiment. A custom script used the EVM algorithm to extract the RR of the mouse under anesthesia from the video.

Detailed signal processing algorithms

The signal processing algorithms used custom Python scripts with Python 3.8.10, Scipy 1.7.3, Numpy 1.20.2, Pandas 1.2.5, Tensorflow 2.4, and Matplotlib 3.3.4 packages. The detailed algorithms were as follows: (1) HR calculation: Subtracting the motion component estimated by Savitzky-Golay filtering (8th order and 21-point filter window) from the raw z-axis acceleration yielded the heart sounds. The Shannon energy envelope of these sounds after low-pass filtering (cut-off frequency: 15 Hz) yielded smoothed heartbeats.[43,44] The automatic multiscale-based peak detection (AMPD) algorithm for quasi-periodic peak detection identified the heartbeats.[45] Based on the mean beat-to-beat interval in each window (1 s unless otherwise specified), the number of heartbeats per minute yielded the HR (unit: BtPM). (2) RR calculation: The envelope of the amplitudes of detected heartbeats after bandpass filtering (frequency range: 1 – 4 Hz) yielded the waveform of respiration cycles. The AMPD algorithm detected the respiration cycles. Based on the mean interval between respiration cycles in each window, the number of respiration cycles per minute was calculated as the RR (unit: BrPM). (3) SQI calculation: The normalized first non-zero-lag peak of the autocorrelation of the cleaned heart sounds defined the SQI. (4) PA calculation: The calculation started with decimation of x-, y-, z-axis accelerations to 50 Hz. The decimated 3-axis accelerations were segmented to 2 s windows. The window average of the low-frequency band-limited (1 – 25 Hz) RMS of 3-axis accelerations defined the PA. (5) Behavioral classification: The decimated 3-axis accelerations of each window (2 s at 50 Hz), vertically stacked to a shape of 3×100, served as the input feature for behavioral classification. The classification utilized a CNN model sequentially consisting of a 32-layer convolution with a kernel size of 4×3, a 3×3 max pooling layer, a dropout layer (p=0.1), a 64-layer convolution with a kernel size of 4×1, a 3×1 max pooling layer, a dropout layer (p=0.1), a flattening layer, a fully

connected layer with 64 neurons at the output, and a fully connected layer with 6 neurons at the output. Training of the CNN model involved 20 hours of hand-scored MA signals (36,000 samples) augmented by Gaussian-noise to a total 100,000 samples. The hand-scoring process involved expert labeling of the videos synchronized with the MA signals using the BORIS software. Hand-scoring results by 3 independent expert scorers were cross-checked to yield the final labels for training. The hand-scored data were randomly split into 2 datasets of 80 %: 20 % for training and testing, respectively. Each training dataset used a 5-fold cross-validation for training and validation purposes. The training used an Adam optimizer.

Open-field test and motion tracking

The test used 9 adult male CD1 mice. The open-field test used a cage with dimensions of 30 cm × 20 cm × 20 cm (length × width × height). The testing involved non-implanted, untethered mice (n = 3), non-implanted, tethered mice (n = 3), and implanted mice (n = 3). The mice freely explored the open-field enclosure for 10 min under low-light conditions (50 lx). An overhead camera (acA1920-25gc, Basler AG, Germany) recorded the motions of the mice at 25 frames per second. Subsequent motion analysis utilized a deep learning model trained by DeepLabCut.[64] Manually labeling 2 body parts (head and tail) in 1,000 representative frames generated a training set for a pre-trained CNN. Training the CNN for 100,000 epochs yielded the deep learning model that detected the head and tail of the mouse frame by frame. The corresponding trajectories of the head served as the basis for determining the head speed and total travel distance of the mice as well as the time spent in the inner zone (defined as the central 25 % area of the cage).

Pharmacological test

The test used a total of 6 adult CD1 mice, 3 males and 3 females. Each mouse was given saline as a control then after 24 hours given Atenolol (10 mg kg^{-1}). After another 24 hours the mice would receive Carvedilol (10 mg kg^{-1}). All drugs were administered intraperitoneally. The recording of MA signals started at 2 hours after injection and lasted for 20 min.

Running wheel test

The test used 5 adult male CD1 mice that had no prior exposure to a running wheel. Each mouse was habituated in the test cage for at least 30 min, followed by recording MA signals at baseline for at least 10 min. After the placement of a running wheel in the cage, the recording of MA signals continued for 30 min.

Forced swim test

The test used a total of 14 adult CD1 mice, 7 males and 7 females. The experimental setup involved a cylindrical glass water tank half-filled with room-temperature water and encircled by a double-loop primary antenna for WPT. After placement of the mouse in the water tank, the recording of MA signals continued for 20 min.

Shock grid test

On Day 1, mice were trained to associate an auditory tone with a shock delivery. Mice were placed in the shock grid chamber and habituated for 2 hr before the fear conditioning session. During fear conditioning, mice were presented with 30 trials in which a 10-s tone cue (3 kHz, 90 dB) predicted the delivery of a 2-s shock (0.5 mA). The shock was delivered at the end of the predicting tone. To indicate the predicting tone in recorded videos, a dim red light emitting diode (LED) that co-activated and terminated with the predictive tone was placed outside of the shock grid chamber. The trial interval was fixed at 2 min and 15 s. Once the 30 trials were completed, the mouse was returned to its home cage. On Day 2, the mouse was placed in a regular testing cage (30 cm × 20 cm × 20 cm) and habituated for 2 hr. Mice were presented with tones only and no shocks for 30 trials, with the same parameters as those on Day 1. Once the 30 trials were completed, the mouse was returned to its home cage.

Resident-intruder test

The test used a total of 3 adult male CD1 resident mice implanted with the MA device and 3 adult male CD1 intruder mice (not implanted). A perforated, transparent partition divided the testing cage in the middle. Each resident mouse habituated in the left chamber for at least 30 min, followed by recording MA signals at baseline for at least 10 min. After the addition of an intruder mouse to the right chamber, the two mice interacted for 5 min in the presence of the partition. Next, after the removal of the partition, the two mice physically interacted for no more than 5 min. The experimenters monitored the interactions and removed the intruder upon noticing potential severe injury. After the removal of the intruder, the MA recording of the resident continued for 30 min.

Witness defeat test

The test used a total of 8 adult CD1 mice, 4 male and 4 female witnesses. A perforated, transparent partition divided the testing cage in the middle. The left chamber houses a witness mouse (CD1, implanted, male/female) that observed the interactions between the resident (CD1, male) mouse and intruder (C57BL/6, male) mouse in the right chamber throughout the test, without any physical interaction with the resident and intruder. Each witness mouse habituated in the left chamber for at least 30 min, followed by recording MA signals at baseline for at least 10 min. The test included the following five phases: 1) Witness only, 2) Addition of the resident to the right chamber, 3) Addition of the intruder to the right chamber, 4) Removal of the intruder from the right chamber, and 5) Removal of the resident from the right chamber. After the removal of the resident, the MA recording of the witness continued for 30 min.

Chronic recording

The test used 1 adult male CD1 mouse fed ad libitum in a 30 cm × 20 cm × 20 cm (length × width × height) cage encircled by a double-loop primary antenna for WPT. The room was climate controlled and under 12 hr light-dark cycles (6 am – 6 pm: light; 6 pm – 6 am: dark). Trained personnel cleaned the cage and replenished food and water daily.

Stereotactic injections

For intracranial injections, 6 male C57BL/6 mice (~30g) were anesthetized with isoflurane (3 % for induction, 1.5-2 % for maintenance) and administered bupivacaine and meloxicam pre-surgery for analgesia. The animals were then positioned in a small animal stereotaxic frame (David Kopf Instruments, Tujunga, CA) and their heads leveled for stereotaxic accuracy. A surgical drill was used to create a small burr hole above the right secondary motor cortex (M2; anterior/posterior -2.2 mm, medial/lateral +1.0 mm). Adeno-associated virus (AAV) AAV1.Syn-ChrimsonR-tdT (1×10^{13} GC/mL, Addgene viral prep #59171-AAV1, a gift from Dr. Edward Boyden), was delivered through a pulled glass pipette at a rate of 100-150 nL/min for a total amount of 200 nL (dorsal/ventral -1.0 mm), using an UltraMicroPump (World Precision Instruments, Sarasota, FL). Buprenorphine-ER was administered post-operatively for prolonged analgesia. Viral vectors were allowed to express for at least 4 weeks before implantation of the transcranial optogenetic and ventral MA devices.

Transcranial device implantation

Transcranial optogenetic device implantation followed the procedure reported previously.[59] An incision was made at the midline of the scalp to expose the skull. A surgical drill was used to thin the skull and create a smooth surface over the previous AAV injection site. The transcranial device was submerged in 70 % alcohol for 5 minutes prior to implantation, rinsed with sterile water, then secured to the skull using dental cement. The microscale LED pad was attached to the thinned skull using cyanoacrylate adhesive (KG58548R). Animals were monitored and allowed to recover for several hours before being transferred back to the colony for appropriate post-surgical care and monitoring.

Optogenetic behavioral testing

Animals implanted with transcranial optogenetic and MA devices were transferred from the vivarium to a behavioral room for testing. Following 60 minutes of acclimation and baseline physiological recording, transcranial optogenetic stimulation (20 Hz, 2 % duty cycle, 10 s) was programmed to induce rotational activity. This stimulation paradigm was repeated once every 10 min for up to 10 trials per day of stimulation.

QUANTIFICATION AND STATISTICAL ANALYSIS

For all comparisons in this manuscript, we describe the number of n's, what the n represents, the statistical test used, and the definition of error bars in the figure legend. The details of statistics are listed in the results section. Comparisons were considered to have reached statistical significance if the p-value was less than 0.05, unless otherwise stated. The p-values that correspond to asterisks are listed in the figure legends. For comparison between two groups, a paired two-sided t-test was used.